

See discussions, stats, and author profiles for this publication at: <https://www.researchgate.net/publication/277880848>

Modeling Pressure Stability and Contact-Angle Hysteresis of Superlyophobic Surfaces Based on Local Contact Line

ARTICLE *in* THE JOURNAL OF PHYSICAL CHEMISTRY C · MAY 2015

Impact Factor: 4.77 · DOI: 10.1021/jp512930d

READS

21

2 AUTHORS:



[Zhiwei Wang](#)

Chinese Academy of Sciences

11 PUBLICATIONS 19 CITATIONS

SEE PROFILE



[Tianzhun Wu](#)

Chinese Academy of Sciences

34 PUBLICATIONS 196 CITATIONS

SEE PROFILE

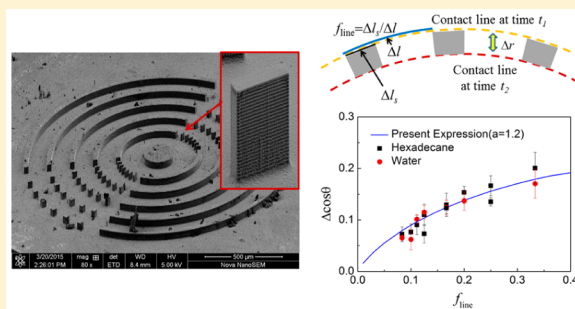
Modeling Pressure Stability and Contact-Angle Hysteresis of Superlyophobic Surfaces Based on Local Contact Line

Zhiwei Wang and Tianzhun Wu*

Shenzhen Institutes of Advanced Technology, Chinese Academy of Sciences, 1068 Xueyuan Avenue, Shenzhen 518055, China

Supporting Information

ABSTRACT: Superlyophobic surfaces (SLS) are a promising versatile platform for planar microfluidics due to their excellent nonwetting and low flow-resistance performances for almost any liquid; however, for micro fabrication and practical application, the nonwetting performances, especially pressure stability and contact-angle hysteresis (CAH), are vital parameters yet still difficult to predict well. On the basis of the Laplace pressure formulation and the pinning condition on typical overhang surface structures, we obtained a universal expression to calculate the critical transition pressure and hence proposed two dimensionless parameters as criteria for the Cassie–Baxter state. We also propose a new model for the CAH of both water and oil on SLS by introducing contact line fraction. The theoretical predications are well supported by the experimental data on the SLS with microfabricated T-shape microstructures. These achievements on modeling SLS pressure stability and CAH may shed new light for designing SLS with better performances for microfluidics and other fields.



1. INTRODUCTION

Superhydrophobic surfaces (SHS), which show high apparent contact angles (CAs) of typically $>150^\circ$ and low contact-angle hysteresis (CAH) for water and other aqueous solutions, have been elaborately investigated in the past decades^{1,2} and have been widely used for various applications.^{3,4} Nevertheless, usually SHS do not repel low-surface-tension liquids (typical surface tension 15–35 mN/m) such as oil, organic solutions, and aqueous solutions with surfactants.⁵ What is more, SHS are apt to be contaminated by oil or organic solutions and lead to degradation of water-repellency.⁶ As an extension and enhancement of SHS, superlyophobic surfaces (SLS) have attracted much interest in recent years.^{7,8} SLS can repel almost any liquid and provide high apparent CAs and low CAH, and hence they can effectively minimize liquid waste, prevent contamination, and reduce flow resistance. Because of their excellent performances, SLS provide a promising versatile platform for the manipulation of almost any kinds of fluids,⁹ no matter high or low surface tension, high or low viscosity, polar or nonpolar, organic or inorganic, or Newtonian or non-Newtonian,¹⁰ and hence enable many potential applications, such as self-cleaning surfaces,¹¹ minimizing liquid–solid contact,¹² precise control of droplet shape and motion,¹³ antibacteria,¹⁴ chemical shielding,¹⁰ and generation of droplet arrays.¹⁵

Despite so many attractive characteristics of SLS, engineering and practical applications of SLS are still rare, which are supposed to be limited in two major aspects. One is the fabrication challenge and typical high cost for the overhang micro/nano structures. As a solution, we recently proposed a facile and inexpensive microfabrication approach for high-

performance and mass-production of SLS on various curable materials.⁵ The other one is the lack of proper theoretical model to well predict nonwetting performances, such as static and dynamic CAs, pressure stability, and so on. According to the surface geometries, SLS can have regular structures^{5,6,9,16,17} or random structures;^{18–20} however, even for SLS with regular structures, there are no comprehensive models by far to convincingly predict the nonwetting performances.^{8,21,22}

One impressive characteristic of SLS is their extremely high CAs for various liquids. There are basically two approaches to increase the CA: surface modification using low surface-energy materials or proper roughness with micro/nano structures. Clearly low surface energy treatment alone is insufficient to obtain superhydrophobicity,²³ not to mention superlyophobicity, and hence involving micro/nano surface structures is vital in designing SLS. The micro/nano structures determined the microscopic topology of solid–liquid or solid–liquid–vapor interface, which have crucial effect on the wettability and pressure stability. It is found that the overhang micro/nano structures are beneficial to repel liquid because liquid can be pinned^{6,24} to form the Cassie–Baxter state,²⁵ even on intrinsically hydrophilic materials.²⁶ Recent investigation even demonstrated that specific micro/nano structures alone can render the surface superlyophobic;²⁷ however, to effectively prevent the transition from the Cassie–Baxter state to the Wenzel state, micro/nano structures must be carefully designed

Received: December 27, 2014

Revised: May 9, 2015

Published: May 18, 2015

with sufficient pressure stability to withstand pressure imposed on liquids. Rijke²⁸ first estimated the minimal pressure required for water to penetrate between the parallel cylindrical barbs of birds' feathers. After that, some literature reporting the criterion or modeling for robust SLS has been reported.^{17,20,24,29–32} Tuteja et al.²⁴ defined two parameters, the robustness height H^* and the robustness angle T^* , to predict the breakthrough pressure of surface structures and then further proposed a composite robustness factor A^* to characterize the robustness of any composite surfaces; however, they only derived models applicable to cylindrical re-entrant surface such as electrospun fiber, electrospun beads, and discrete microhoooods. Nhung Nguyen et al.³³ proposed a model to predict the critical impalement pressure by simply assuming the curvature radius is a linear function of pillar space and pillar length. Zhao et al.³⁴ studied the effects of surface chemistry, pillar size, and spacing on the wettability against the breakthrough pressure using the Surface Evolver simulation. In a previous study,⁹ we introduced a normal stress to represent the solid–liquid interaction and proposed two dimensionless factors to predict the wetting state on SLS with verification of experimental data; however, until now, there is still no universal expression for various micro/nano layouts, and the pressure stability prediction of SLS is still difficult.

Besides the high CA, another remarkable advantage of SLS is their low CAH for almost any liquid. CAH, defined as the differences between the cosine of the threshold receding CA and the threshold advancing CA, is important for the practical application because it corresponds to the flow resistant force. It is now widely recognized that static and dynamic CAs depend on the three-phase contact line (TCL) in the vicinity of the contact line other than the global micro/nano dimensions.^{35–38} Effective simulation of the dynamic contact angle at the three-phase contact is still in its infancy,³⁹ and hence surfaces with specific layouts are designed for the CAH investigation;^{40–42} however, except for some literature that discussed CAH on the basis of contact line density,^{43,44} which is defined as the length of the asperity perimeter per unit area, most existing CAH models or discussions are based on the widely used dimensionless parameter called solid fraction f_s ,^{36,42,45–47} defined by the ratio of projected wet area to the unit area. A classical CAH model is proposed by de Gennes^{48,49} and developed by Reyssat and Quéré,⁴⁶ in which a spring stiffness is introduced to quantitatively characterize the energy stored in the distorted TCL. They demonstrated the analytical expression could fit experimental results well on sparse cylindrical pillar arrays with a given distortion coefficient; however, the model was still based on f_s and cannot be extended to nonuniform structures.

In conclusion, there is still no reliable approach to evaluate the pressure stability and CAH based on the micro/nano structure dimensions by far. Herein we propose a universal expression to predict the maximum Laplace pressure on SLS with various overhang structures, based on which a criterion to predict the pressure stability of SLS was presented by introducing two dimensionless parameters. We also modify the spring model initialized by de Gennes to predict the CAH on SLS by introducing the local contact line fraction.

2. PRESSURE STABILITY ANALYSIS OF SLS

As shown in Figure 1, many of random or uniform micro/nano structures, such as electrospun fiber structure,^{6,10} “T” structure,^{16,21} mushroom structure,⁵⁰ inverted trapezoid

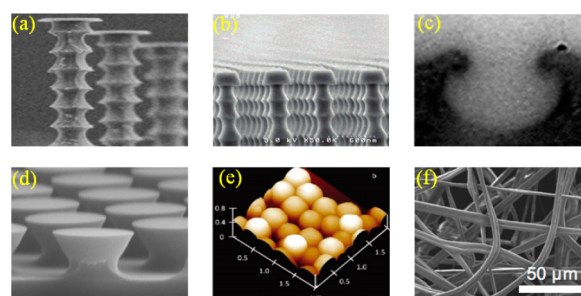


Figure 1. Typical microstructures of superlyophobic surfaces. (a) “T” structures,²¹ (b) nail structures,¹⁶ (c) mushroom structures,⁵⁰ (d) inverted trapezoid structures,⁵² (e) sphere structures,⁵³ and (f) electrospun fiber structures.⁶

structure,^{51,52} sphere structure,^{53,54} and so on., can be fabricated.⁷ According to the design criteria of SLS, several requirements,^{21,55–57} such as overhang surface structure, pinning condition, curvature requirement, and suspending condition, should be satisfied. In the Cassie–Baxter state, the hydrostatic pressure and downward Laplace pressure induced by the convex droplet top are balanced by upward Laplace pressure originated from the micro/nano liquid menisci on the bottom.²¹ For the transition from the Cassie–Baxter state to the Wenzel state, there are two failure modes for SLS,⁵¹ T^* failure and H^* failure. The former represents the scene that local contact line slides down along the side wall, while the latter is caused by the bending liquid curvature that touches the bottom of structure and leads to full wetting. Essentially, H^* failure mode can be avoided by fabrication improvement to provide sufficient height and stiffness of micro/nano structures. Hence, the key issue in improving the pressure stability is to prevent T^* failure. According to Laplace pressure equation $P_{La} = 2\gamma/R$, for a specific liquid, the only way to increase P_{La} is to reduce curvature radius R in the cavity, and hence it is a prerequisite to obtain the expression of R .²⁸

Ideally, R is determined by geometric dimensions of structures⁵⁸ and the maximum pinning angle, which is constrained by the Gibbs inequalities.²¹ Because the concave profile has been reported to be unstable,⁵⁵ there are three different types of side profiles for overhang micro/nano structures (vertical, incline, and convex), as shown in Figure 2. The pinning of liquid on these structures is analyzed separately. For the case of pinning on upper edge of T

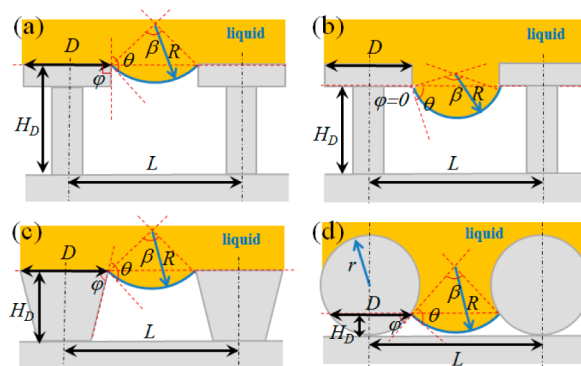


Figure 2. Pinning of contact line on typical overhang microstructures. (a) Pinning on upper edge of “T” structures, (b) pinning on lower edge of “T” structures, (c) pinning on inverted trapezoid structures, and (d) pinning on sphere structures.

structures in Figure 2a, the slope angle, defined as intersection angle between the horizontal surface and the local TCL, $\varphi = \pi/2$. The central angle β , which is the angle corresponding to the liquid interface arc, can be expressed as

$$\beta_{TU} = 2(\theta - \pi/2) = 2(\theta - \varphi) \quad (1)$$

While for the case of pinning on lower edge in Figure 2b, $\varphi = 0$, and β can be expressed as

$$\beta_{TL} = 2(\theta - \varphi) \quad (2)$$

Also, for the case of pinning on inverted trapezoidal structures in Figure 2c, β can be expressed as

$$\beta_{IT} = 2(\pi/2 - (\varphi - (\theta - \pi/2))) = 2(\theta - \varphi) \quad (3)$$

As for the case of pinning on sphere structures in Figure 2d, β can be expressed as

$$\beta_{SP} = 2(\pi/2 - \varphi + (\theta - \pi/2)) = 2(\theta - \varphi) \quad (4)$$

As the conclusion, for the overhang micro/nano structures mentioned above, there exists a universal expression

$$\beta = 2(\theta - \varphi) \quad (5)$$

Hence the curvature radius R can be expressed as

$$R = \frac{L/2 - D/2}{\sin(\beta/2)} = \frac{L - D}{2\sin(\theta - \varphi)} \quad (6)$$

Therefore, we obtain a universal expression to calculate the maximum Laplace pressure

$$P_{La,max} = 2\gamma \left[\frac{\sin(\theta_x - \varphi_x)}{(L_x - D_x)} + \frac{\sin(\theta_y - \varphi_y)}{(L_y - D_y)} \right] \quad (7)$$

where L and D are, respectively, the pitch distance and cap size of the micro/nano structures and the subscripts x and y represent two principal directions.

According to the Gibbs inequalities,²¹ the pinning angle θ in Figure 2 is confined by the Young's CA, $\theta \leq \theta_Y$. Considering that Laplace pressure is the only upward force supporting the droplet, θ should be larger than φ , to form a convex meniscus liquid–gas interface in the micro/nano cavity. Therefore

$$\varphi < \theta \leq \theta_Y \quad (8)$$

which is consistent with the previous report on Si-based superhydrophobic surfaces,²⁶ where θ_{overhang} corresponds to φ and θ_{flat} corresponds to θ .

For the two failure modes, namely, T^* failure and H^* failure,⁵¹ we proposed two dimensionless parameters as criteria to predict the failure modes of Cassie–Baxter state droplet: $P^* = \ln(P_{La,max}/P_{\text{down}})$ for the T^* failure, where $P_{\text{down}} = \rho g h_{\text{drop}} + 2\gamma/r$ is the summation of hydrostatics pressure and downward Laplace pressure due to the macroscopic droplet shape⁹ and $H^* = \ln(H_D/H_S)$ for the H^* failure, where h_{drop} and r are the height and radius of droplet and H_D and H_S are the actual height of micro/nano structures and the maximum suspension height of liquid, respectively. Clearly the necessary but insufficient condition for the Cassie–Baxter state should be $P^* > 0$ and $H^* > 0$. Given the universal expression of curvature radius R in eq 6, the maximum suspension height of liquid H_S can be expressed as

$$H_S = R(1 - \cos(\beta/2)) = (L - D) \frac{1 - \cos(\theta - \varphi)}{2\sin(\theta - \varphi)} \quad (9)$$

For the “T” shape and inverted trapezoid micro/nano structures, H_D can be obtained from the geometry of the structure, as seen in Figure 2, while for sphere structure H_D can be expressed as $H_D = r(1 - \cos \varphi)$. In the expression r is the radius of the sphere structure, while φ can be varied from 0 to the smaller value of Young's angle and $\pi/2$. Typically the liquid interface is pinned at lower position with a small φ value and hence H_D is small compared with r .

To validate the pressure stability analysis above, we fabricated T-shape micro structures SLS on Si substrate using deep reactive ion etching (DRIE), as shown in Figure 3a. By

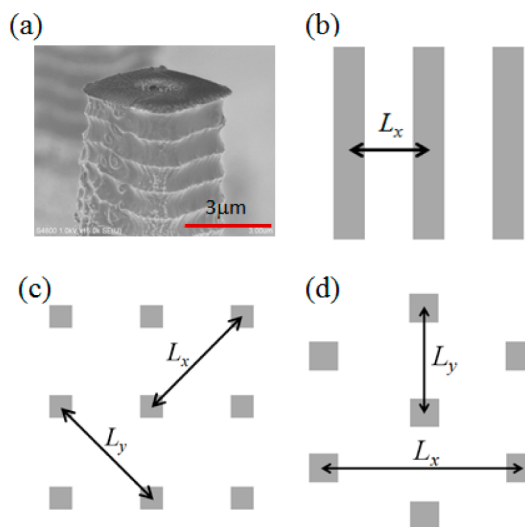


Figure 3. Geometric layouts fabricated by deep reactive ion etching on Si used for pressure stability analysis. (a) SEM images of a typical SLS micro structure with a slight undercut. (b) Linear, (c) square, and (d) hexagonal layouts of the SLS micro structures.

optimizing DRIE process conditions, highly uniform overhang structures with small undercuts (~ 300 nm) were achieved.²¹ Linear, square, as well as hexagonal patterns with a series of different cap sizes and pitch distances were fabricated in Figure 3b–d, and the cap sizes and pitch distances are listed in Table 1. Deionized water ($\gamma = 73$ mN/m, $\rho = 1000$ kg/m³) with a volume of ~ 5 μ L and hexadecane ($\gamma = 27$ mN/m, $\rho = 770$ kg/m³) with a volume of ~ 2 μ L were used as probe liquids. A drop-shape analysis system (KRUS, DSA 25) fixed on a vibration-free lab table (TMC 63–521) was used to monitor the droplet wetting state. In each experiment, droplets were dropped onto the superhydrophobic surface closely and carefully to minimize the effect of droplet impact (see supplement videos in the Supporting Information for the experimental process).

We assume the fabricated microstructures are perfect T-shape, and hence deionized water will be pinned on the upper edge of the T-shape with $\varphi = \pi/2$ and hexadecane will be pinned on the lower edge of the T-shape with $\varphi = 0$. Hence P^* and H^* can be calculated through the geometric dimension of microstructures and Young's CA on the surface. The wetting states of water and hexadecane droplets on various SLS are plotted on Figure 4. For SLS with $H^* < 0$, all of the droplets are in the Wenzel state, which is because the actual etching height of micro/nano structures is smaller than the suspension height of liquid and results in H^* failure. Experimental results indicate droplet can be on the Cassie–Baxter state only when $H^* > 0$ and $P^* > 2$, which is because SLS with a small P^* is fragile to disturbances acting on the droplet and effective pressure of

Table 1. Parameters of the Fabricated Linear, Square, and Hexagonal Patterns for the Pressure Stability Analysis

layout no.	pattern	x direction (μm)		y direction (μm)	
		cap size D	pitch distance L	cap size D	pitch distance L
1	linear	3	30	/	/
2	linear	3	90	/	/
3	linear	3	240	/	/
4	linear	3	300	/	/
5	hexagonal	3	30	3	52
6	hexagonal	3	33	3	57
7	hexagonal	3	36	3	62
8	hexagonal	3	39	3	68
9	hexagonal	30	240	30	416
10	hexagonal	30	270	30	468
11	hexagonal	30	300	30	520
12	hexagonal	30	360	30	624
13	square	3	30	3	30
14	square	3	33	3	33
15	square	3	36	3	36
16	square	3	39	3	39
17	square	30	240	30	240
18	square	30	270	30	270
19	square	30	300	30	300
20	square	30	360	30	360

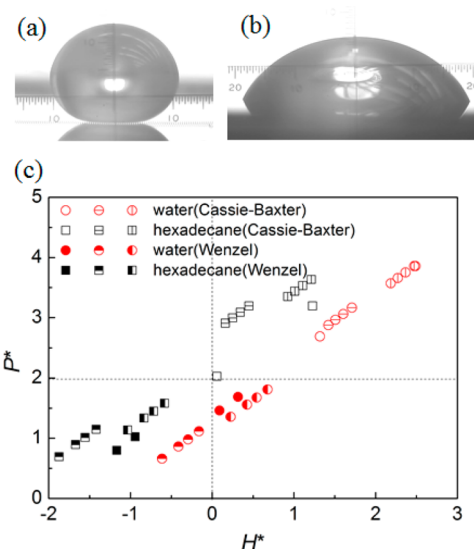


Figure 4. Wetting state of droplets on SLS of linear, square and hexagonal layouts for different P^* and H^* . (a) Typical Cassie–Baxter state. (b) Typical Wenzel state. (c) Experimental results indicate the droplet can be on the Cassie state only when $H^* > 0$ and $P^* > 2$. Red \circ , red \bullet , \square , and \blacksquare for the linear layouts. Red \ominus , red \odot , square with horizontal bar, and \boxplus for the square layouts. Red \oplus , red \otimes ; square with vertical bar, and \boxtimes for the hexagonal layouts.

droplet impact. Hence the droplets on such SLS tend to irreversibly transition from the Cassie–Baxter state to the Wenzel state. Therefore, P^* should be sufficiently large for robust SLS.

3. CONTACT-ANGLE HYSTERESIS ANALYSIS OF SLS

A widely used CAH model was proposed by Reyssat and Quéré⁴⁶ by investigating the contact angle hysteresis generated by strongly dilute defects and introducing the spring stiffness to quantitative characterize the energy stored in the distorted TCL, expressed as

$$\Delta \cos \theta = a/4f_s \ln(\pi/f_s) \quad (10)$$

where a is a coefficient depending on the detail of the line distortion, and their experimental results on strongly dilute cylindrical pillar arrays suggested $a = 3.8$.⁴⁶

Considering the fact that surfaces with the same f_s and different TCL exhibit different advancing and receding contact angles,⁵⁹ we suppose the existing CAH models may fail for nonuniform surfaces. Hence we fabricated SLS of uniformly distributed and nonuniformly distributed discrete-ring layouts with different δ and $\Delta\delta$ (see Figure 5). The discrete-ring

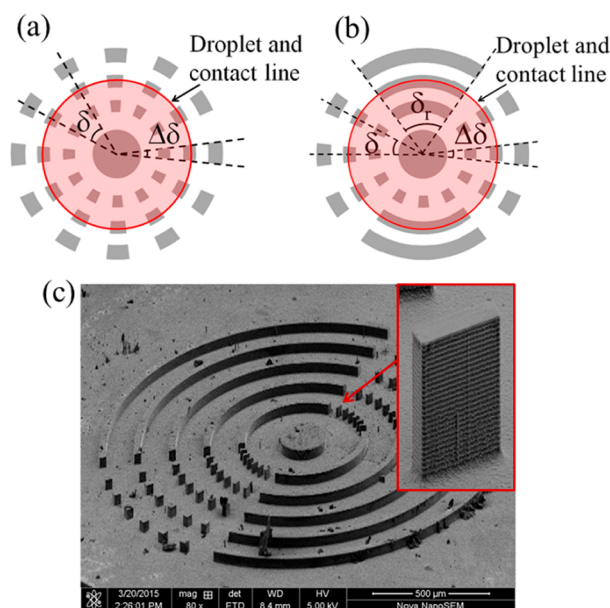


Figure 5. Geometric layouts used for contact-angle hysteresis analysis. (a) Uniformly distributed and (b) nonuniformly distributed discrete-ring layouts. (c) SEM image of a typical nonuniformly distributed discrete-ring layouts.

layouts depicted in Figure 5 were designed for the TCL investigation, which is inspired by the pioneer work of Johnson and Dettre.⁶⁰ Detailed parameters of different layouts are listed in Table 2. Contact areas of droplet on the layouts are circular;

Table 2. Parameters of the Fabricated Uniformly Distributed and Non-Uniformly Distributed Discrete-Ring Layouts for Contact Angle Hysteresis Analysis

layout no.	post part		ridge part		f_s	f_{line}
	δ (deg)	$\Delta\delta$ (deg)	δ_r (deg)	number (—)		
1	6	2	0	0	0.069	0.333
2	12	2	0	0	0.046	0.167
3	18	2	0	0	0.038	0.111
4	24	2	0	0	0.034	0.083
5	6	3	0	0	0.193	0.500
6	15	3	0	0	0.115	0.200
7	24	3	0	0	0.095	0.125
8	30	3	0	0	0.089	0.100
9	8	2	0	0	0.106	0.250
10	8	2	60	2	0.159	0.250
11	12	2	60	2	0.147	0.167
12	16	2	120	2	0.178	0.125

therefore, it is easy to obtain the line proportion of TCL along the contact perimeter on the layouts. In the present experiments, for each sample, contact angles were measured at least 10 times with a drop-shape analysis system (KRUS, DSA 25) in the laboratory environment (23 ± 2 °C, humidity $50 \pm 5\%$) with a standard deviation of $<2^\circ$. Advancing and receding contact angles are obtained by adding or decreasing liquid volumes.

We found that eq 10 failed to fit our experimental results by varying the value of a , as can be seen in Figure 6, which indicates the inapplicability of the model of Reyssat and Qu  r   on the discrete-ring layouts in Figure 5.

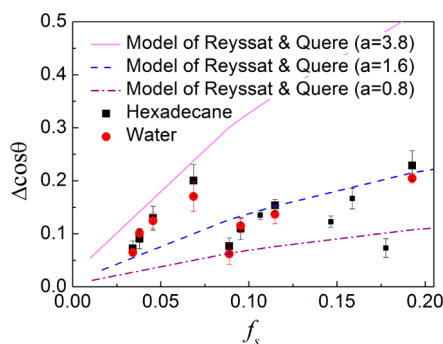


Figure 6. Relation between the area fraction f_s and measured CAH on the SLS of discrete-ring layouts.

Hence we propose a new model based on the correlation between CAH and TCL. For the unit microstructure with length Δl shown in Figure 7, the flow resistance caused by CAH acts on the solid part Δl_s only, and hence we have

$$F_t = \gamma \Delta \cos \theta \Delta l_s \quad (11)$$

Denoting ϵ as the maximum energy stored in unit microstructure with length Δl , the force represented by the energy stored in the distorted TCL can be expressed as

$$F_s = \epsilon / \Delta l \quad (12)$$

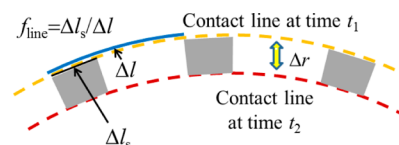


Figure 7. Definition of contact line fraction f_{line} and the contact line motion for the discrete-ring layouts in Figure 5.

Ideally flow resistance should be equal to F_s , so we have

$$\gamma \Delta \cos \theta \Delta l_s = \epsilon / \Delta l \quad (13)$$

For dilute and small micro/nano structures, we have $\Delta l_s \ll \Delta l$ and $\Delta l \ll R$. So referring to the analysis of Reyssat and Qu  r  ,⁴⁶ the deformation of contact line can be written as

$$y = \Delta l_s / 2 \cosh(2u / \Delta l_s) \approx 1/4 \Delta l_s \exp(2u / \Delta l_s) \quad (14)$$

where the deformation u yields a maximum value when $y = \Delta l / 2$, yielding

$$u \approx \Delta l_s \ln(2\Delta l / \Delta l_s) / 2 \quad (15)$$

The force on each microstructure can be written as $f = a \Delta l_s \gamma$, where a is a coefficient depending on the detailed line distortion, which is similar to eq 10.⁴⁶ Considering eq 15, $\Delta l_s \approx 2u / \ln(2\Delta l / \Delta l_s)$, and thus we have

$$f = 2a\gamma u / \ln(2\Delta l / \Delta l_s) = [2a\gamma / \ln(2\Delta l / \Delta l_s)]u = Ku \quad (16)$$

where $K = 2a\gamma / \ln(2\Delta l / \Delta l_s)$ is the stiffness of the "liquid spring".^{46,48} Hence the energy stored in unit micro structure can be expressed as

$$\epsilon = 1/2 Ku^2 = 1/4 a\gamma \Delta l_s^2 \ln(2\Delta l / \Delta l_s) \quad (17)$$

We define the contact line fraction f_{line} as

$$f_{line} = \Delta l / \Delta l_s \quad (18)$$

then from eq 13, we can obtain the following expression to predict the CAH of SLS

$$\Delta \cos \theta = a/4 f_{line} \ln(2/f_{line}) \quad (19)$$

The relation between f_{line} and CAH are plotted on Figure 8, in which the prediction from eq 19 fits the measured CAH results fairly well when $a = 1.2$. It is important to note here for the nonuniformly distributed discrete-ring layouts depicted in Figure 5b that f_{line} should be the local value. The good agreement with our experimental data indicates the fact the

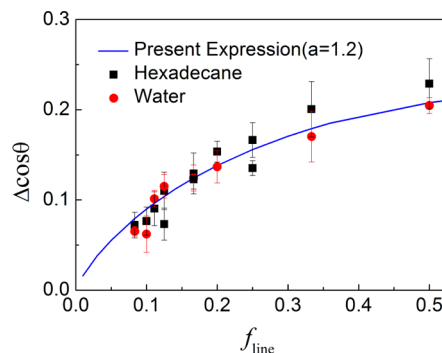


Figure 8. Relation between local f_{line} and measured CAH. Prediction from present analytical expression eq 19 fits the results fairly well when $a = 1.2$.

CAH depends on the local contact line fraction and detailed line distortion only, with little influence on the liquid surface tension.

Although eq 19 is derived from the uniformly distributed and nonuniformly distributed discrete-ring layouts, the expression should be valid on various regular or random layouts provided the contact line fraction f_{line} can be calculated accurately; however, we should note that eq 19 is still confined by the assumption of dilute micro/nano structures. In the analysis of Reyssat and Quéré, f_s should be <0.3 ; otherwise, their experimental results significantly deviated from the theoretical prediction. In the present analysis, f_{line} is used instead of f_s , and it should be smaller than ~ 0.55 , which is the square root of 0.3 ($0.3^{1/2} \approx 0.55$).

4. CONCLUSIONS

We modeled the pressure stability and CAH from the aspect of local contact line to exactly predict the wetting performance of SLS with various micro/nano structures.

First, we derived a universal expression for the first time to predict the maximum Laplace pressure on various typical overhang micro/nano structures; then, based on the expression we further investigated the pressure stability on SLS. By introducing two dimensionless parameters, P^* and H^* , a criterion for SLS was established and validated by experimental data on Si substrate.

Second, we designed SLS with various uniformly and nonuniformly distributed discrete-ring layouts to obtain the simplified TCL and analyzed the relationship between local contact line and contact angle. By introducing contact line fraction f_{line} , we modified the CAH model of Reyssat and Quéré based on solid fraction f_s , which failed to give a meaningful fit for our experimental data, and proposed a new model by introducing contact line fraction. The formulation is in a good agreement with the measured CAH results when $a = 1.2$ for both water and hexadecane on SLS with various discrete-ring layouts.

We anticipate that these models can be helpful in quantitative prediction and evaluation of SLS nonwettability by exploring the underlying microscopic solid–liquid interaction details. They may also shed new light for design and fabrication of high-performance SLS for practical applications.

■ ASSOCIATED CONTENT

Supporting Information

Two video clips showing Cassie–Baxter state and Wenzel state of hexadecane droplet. These materials are available free of charge via the Internet at The Supporting Information is available free of charge on the ACS Publications website at DOI: 10.1021/jp512930d.

■ AUTHOR INFORMATION

Corresponding Author

*E-mail: tz.wu@siat.ac.cn. Phone: +86-(755) 8639-2339.

Notes

The authors declare no competing financial interest.

■ ACKNOWLEDGMENTS

This research was supported by National Natural Science Foundation of China (Nos. 51105388, 51406221, 51475451), China Postdoctoral Science Foundation funded project (No. 2014M552253), Guangdong Innovative and Entrepreneurial

Research Team Program (No. 2013S046), Guangdong Natural Science Foundation (No. 2014A030310138), Shenzhen Peacock Plan (No. 20130409162728468), and Shenzhen Basic Research Project (No. JCYJ20140417113430581).

■ REFERENCES

- (1) Sanjay, S. L.; Annaso, B. G.; Chavan, S. M.; Rajiv, S. V. Recent progress in preparation of superhydrophobic surfaces: a review. *J. Surf. Eng. Mater. Adv. Technol.* **2012**, *2* (2), 76–94.
- (2) Celia, E.; Darmanin, T.; Taffin de Givenchy, E.; Amigoni, S.; Guittard, F. Recent advances in designing superhydrophobic surfaces. *J. Colloid Interface Sci.* **2013**, *402*, 1–18.
- (3) Bhushan, B.; Jung, Y. C. Natural and biomimetic artificial surfaces for superhydrophobicity, self-cleaning, low adhesion, and drag reduction. *Prog. Mater. Sci.* **2011**, *56* (1), 1–108.
- (4) Chen, Y.; Xu, J.; Guo, Z. Recent Advances in Application of Biomimetic Superhydrophobic Surfaces. *Prog. Chem.* **2012**, *24* (5), 696–708.
- (5) Yuan, L.; Wu, T.; Zhang, W.; Ling, S.; Xiang, R.; Gui, X.; Zhu, Y.; Tang, Z. Engineering superhydrophobic surfaces on curable materials based on facile and inexpensive microfabrication. *J. Mater. Chem. A* **2014**, *2* (19), 6952–6959.
- (6) Tuteja, A.; Choi, W.; Ma, M.; Mabry, J. M.; Mazzella, S. A.; Rutledge, G. C.; McKinley, G. H.; Cohen, R. E. Designing Superoleophobic Surfaces. *Science* **2007**, *318* (5856), 1618–1622.
- (7) Liu, K.; Tian, Y.; Jiang, L. Bio-inspired superoleophobic and smart materials: Design, fabrication, and application. *Prog. Mater. Sci.* **2013**, *58* (4), 503–564.
- (8) Bellanger, H.; Darmanin, T.; Taffin de Givenchy, E.; Guittard, F. Chemical and Physical Pathways for the Preparation of Superoleophobic Surfaces and Related Wetting Theories. *Chem. Rev.* **2014**, *114* (5), 2694–2716.
- (9) Wu, T.; Suzuki, Y. Engineering superhydrophobic surfaces as the microfluidic platform for droplet manipulation. *Lab Chip* **2011**, *11* (18), 3121–3129.
- (10) Pan, S.; Kota, A. K.; Mabry, J. M.; Tuteja, A. Superomniphobic Surfaces for Effective Chemical Shielding. *J. Am. Chem. Soc.* **2013**, *135* (2), 578–581.
- (11) Kim, T.-i.; Tahk, D.; Lee, H. H. Wettability-controllable super water- and moderately oil-repellent surface fabricated by wet chemical etching. *Langmuir* **2009**, *25* (11), 6576–6579.
- (12) Wu, T.; Suzuki, Y. Liquid Dielectrophoresis on Electret: A Novel Approach Towards CMOS-Driven Digital Microfluidics. *J. Adhes. Sci. Technol.* **2012**, *26* (12–17), 2025–2045.
- (13) Liimatainen, V.; Sariola, V.; Zhou, Q. Controlling Liquid Spreading Using Microfabricated Undercut Edges. *Adv. Mater.* **2013**, *25* (16), 2275–2278.
- (14) Jin, C.; Jiang, Y.; Niu, T.; Huang, J. Cellulose-based material with amphiphobicity to inhibit bacterial adhesion by surface modification. *J. Mater. Chem.* **2012**, *22* (25), 12562–12567.
- (15) Dufour, R.; Brunet, P.; Harnois, M.; Boukherroub, R.; Thomy, V.; Senez, V. Zipping Effect on Omniphobic Surfaces for Controlled Deposition of Minute Amounts of Fluid or Colloids. *Small* **2012**, *8* (8), 1229–1236.
- (16) Ahuja, A.; Taylor, J.; Lifton, V.; Sidorenko, A.; Salamon, T.; Lobaton, E.; Kolodner, P.; Krupenkin, T. Nanonails: A simple geometrical approach to electrically tunable superhydrophobic surfaces. *Langmuir* **2008**, *24* (1), 9–14.
- (17) Im, M.; Im, H.; Lee, J.-H.; Yoon, J.-B.; Choi, Y.-K. A robust superhydrophobic and superoleophobic surface with inverse-trapezoidal microstructures on a large transparent flexible substrate. *Soft Matter* **2010**, *6* (7), 1401–1404.
- (18) Choi, W.; Tuteja, A.; Chhatre, S.; Mabry, J. M.; Cohen, R. E.; McKinley, G. H. Fabrics with Tunable Oleophobicity. *Adv. Mater.* **2009**, *21* (21), 2190–2195.
- (19) Zhang, J.; Seeger, S. Superoleophobic Coatings with Ultralow Sliding Angles Based on Silicone Nanofilaments. *Angew. Chem., Int. Ed.* **2011**, *50* (29), 6652–6656.

- (20) Deng, X.; Mammen, L.; Butt, H.-J.; Vollmer, D. Candle Soot as a Template for a Transparent Robust Superamphiphobic Coating. *Science* **2012**, 335 (6064), 67–70.
- (21) Wu, T.; Suzuki, Y. Design, microfabrication and evaluation of robust high-performance superlyophobic surfaces. *Sens. Actuators, B* **2011**, 156 (1), 401–409.
- (22) Bormashenko, E. Progress in understanding wetting transitions on rough surfaces. *Adv. Colloid Interfac* **2014**, DOI: 10.1016/j.cis.2014.02.009.
- (23) Nishino, T.; Meguro, M.; Nakamae, K.; Matsushita, M.; Ueda, Y. The Lowest Surface Free Energy Based on $-CF_3$ Alignment. *Langmuir* **1999**, 15 (13), 4321–4323.
- (24) Tuteja, A.; Choi, W.; Mabry, J. M.; McKinley, G. H.; Cohen, R. E. Robust Omniphobic Surfaces. *Proc. Natl. Acad. Sci. U.S.A.* **2008**, 105 (47), 18200–18205.
- (25) Cassie, A.; Baxter, S. Wettability of porous surfaces. *Trans. Faraday Soc.* **1944**, 40, 546–551.
- (26) Cao, L.; Hu, H.-H.; Gao, D. Design and Fabrication of Micro-textures for Inducing a Superhydrophobic Behavior on Hydrophilic Materials. *Langmuir* **2007**, 23 (8), 4310–4314.
- (27) Liu, T. L.; Kim, C.-J. C. Turning a surface superrepellent even to completely wetting liquids. *Science* **2014**, 346 (6213), 1096–1100.
- (28) Rijke, A. Wettability and phylogenetic development of feather structure in water birds. *J. Exp. Biol.* **1970**, 52 (2), 469–479.
- (29) Cicely, S.; Noah, M.; Tak-Sing, W.; Philseok, K. Joanna, A. Fabrics coated with lubricated nanostructures display robust omniphobicity. *Nanotechnology* **2014**, 25 (1), 014019.
- (30) Zhang, G.; Lin, S.; Wyman, I.; Zou, H.; Hu, J.; Liu, G.; Wang, J.; Li, F.; Liu, F.; Hu, M. Robust Superamphiphobic Coatings Based on Silica Particles Bearing Bifunctional Random Copolymers. *ACS Appl. Mater. Interfaces* **2013**, 5 (24), 13466–13477.
- (31) Kang, S. M.; Kim, S. M.; Kim, H. N.; Kwak, M. K.; Tahk, D. H.; Suh, K. Y. Robust superomniphobic surfaces with mushroom-like micropillar arrays. *Soft Matter* **2012**, 8 (33), 8563–8568.
- (32) Ganesh, V. A.; Dinachali, S. S.; Nair, A. S.; Ramakrishna, S. Robust Superamphiphobic Film from Electrospun TiO_2 Nanostructures. *ACS Appl. Mater. Interfaces* **2013**, 5 (5), 1527–1532.
- (33) Nhung Nguyen, T. P.; Brunet, P.; Coffinier, Y.; Boukherroub, R. Quantitative Testing of Robustness on Superomniphobic Surfaces by Drop Impact. *Langmuir* **2010**, 26 (23), 18369–18373.
- (34) Zhao, H.; Park, K.-C.; Law, K.-Y. Effect of Surface Texturing on Superoleophobicity, Contact Angle Hysteresis, and “Robustness”. *Langmuir* **2012**, 28 (42), 14925–14934.
- (35) Gao, L.; McCarthy, T. J. How Wenzel and Cassie Were Wrong. *Langmuir* **2007**, 23 (7), 3762–3765.
- (36) Dufour, R.; Harnois, M.; Thomy, V.; Boukherroub, R.; Senez, V. Contact angle hysteresis origins: Investigation on super-omniphobic surfaces. *Soft Matter* **2011**, 7 (19), 9380–9387.
- (37) Bormashenko, E.; Bormashenko, Y. Wetting of Composite Surfaces: When and Why Is the Area Far from The Triple Line Important? *J. Phys. Chem. C* **2013**, 117 (38), 19552–19557.
- (38) Wu, J.; Xia, J.; Lei, W.; Wang, B.-P. Pinning mechanism of advancing sessile droplet on superhydrophobic surfaces. *RSC Adv.* **2014**, 4 (67), 35649–35652.
- (39) Malani, A.; Raghavanpillai, A.; Wysong, E. B.; Rutledge, G. C. Can dynamic contact angle be measured using molecular modeling? *Phys. Rev. Lett.* **2012**, 109 (18), 184501.
- (40) Moradi, S.; Englezos, P.; Hatzikiriakos, S. G. Contact Angle Hysteresis of Non-Flattened-Top Micro/Nanostructures. *Langmuir* **2014**, 30 (11), 3274–3284.
- (41) Dubov, A. L.; Mourran, A.; Moeller, M.; Vinogradova, O. I. Contact angle hysteresis on superhydrophobic stripes. *J. Chem. Phys.* **2014**, 141 (7).
- (42) Raj, R.; Enright, R.; Zhu, Y.; Adera, S.; Wang, E. N. Unified Model for Contact Angle Hysteresis on Heterogeneous and Superhydrophobic Surfaces. *Langmuir* **2012**, 28 (45), 15777–15788.
- (43) Extrand, C. Model for contact angles and hysteresis on rough and ultraphobic surfaces. *Langmuir* **2002**, 18 (21), 7991–7999.
- (44) Extrand, C. W. Criteria for Ultralyophobic Surfaces. *Langmuir* **2004**, 20 (12), 5013–5018.
- (45) Choi, W.; Tuteja, A.; Mabry, J. M.; Cohen, R. E.; McKinley, G. H. A modified Cassie–Baxter relationship to explain contact angle hysteresis and anisotropy on non-wetting textured surfaces. *J. Colloid Interface Sci.* **2009**, 339 (1), 208–216.
- (46) Reyssat, M.; Quéré, D. Contact Angle Hysteresis Generated by Strong Dilute Defects. *J. Phys. Chem. B* **2009**, 113 (12), 3906–3909.
- (47) Xiu, Y.; Zhu, L.; Hess, D. W.; Wong, C. P. Relationship between Work of Adhesion and Contact Angle Hysteresis on Superhydrophobic Surfaces. *J. Phys. Chem. C* **2008**, 112 (30), 11403–11407.
- (48) Joanny, J. F.; de Gennes, P. G. A model for contact angle hysteresis. *J. Chem. Phys.* **1984**, 81 (1), 552–562.
- (49) Raphaël, E.; de Gennes, P. G. Dynamics of wetting with nonideal surfaces. The single defect problem. *J. Chem. Phys.* **1989**, 90 (12), 7577–7584.
- (50) Hensel, R.; Helbig, R.; Aland, S.; Braun, H.-G.; Voigt, A.; Neinhuis, C.; Werner, C. Wetting Resistance at Its Topographical Limit: The Benefit of Mushroom and Serif T Structures. *Langmuir* **2013**, 29 (4), 1100–1112.
- (51) Cavalli, A.; Bøggild, P.; Okkels, F. Parametric Optimization of Inverse Trapezoid Oleophobic Surfaces. *Langmuir* **2012**, 28 (50), 17545–17551.
- (52) Choi, H.-J.; Choo, S.; Shin, J.-H.; Kim, K.-I.; Lee, H. Fabrication of Superhydrophobic and Oleophobic Surfaces with Overhang Structure by Reverse Nanoimprint Lithography. *J. Phys. Chem. C* **2013**, 117 (46), 24354–24359.
- (53) Xiong, D.; Liu, G.; Hong, L.; Duncan, E. J. S. Superamphiphobic Diblock Copolymer Coatings. *Chem. Mater.* **2011**, 23 (19), 4357–4366.
- (54) Hsieh, C.-T.; Wu, F.-L.; Chen, W.-Y. Contact angle hysteresis and work of adhesion of oil droplets on nanosphere stacking layers. *J. Phys. Chem. C* **2009**, 113 (31), 13683–13688.
- (55) Nosonovsky, M.; Bhushan, B. Hierarchical roughness optimization for biomimetic superhydrophobic surfaces. *Ultramicroscopy* **2007**, 107 (10–11), 969–979.
- (56) Kota, A. K.; Mabry, J. M.; Tuteja, A. Superoleophobic surfaces: design criteria and recent studies. *Surf. Innovations* **2013**, 1 (2), 71–83.
- (57) Butt, H.-J.; Semperebon, C.; Papadopoulos, P.; Vollmer, D.; Brinkmann, M.; Ciccotti, M. Design principles for superamphiphobic surfaces. *Soft Matter* **2013**, 9 (2), 418–428.
- (58) Berthier, J.; Loe-Mie, F.; Tran, V. M.; Schoumacker, S.; Mittler, F.; Marchand, G.; Sarrut, N. On the pinning of interfaces on micropillar edges. *J. Colloid Interface Sci.* **2009**, 338 (1), 296–303.
- (59) Gao, L.; McCarthy, T. J. Reply to “comment on how Wenzel and Cassie were wrong by Gao and McCarthy. *Langmuir* **2007**, 23 (26), 13243–13243.
- (60) Johnson, R. E., Jr; Dettre, R. H. Contact angle hysteresis. III. Study of an idealized heterogeneous surface. *J. Phys. Chem.* **1964**, 68 (7), 1744–1750.